

Multiflagellate Swimming Controlled by Hydrodynamic Interactions

Shiyuan Hu^{1,*} and Fanlong Meng^{1,2,3,†}

¹CAS Key Laboratory of Theoretical Physics, Institute of Theoretical Physics, Chinese Academy of Sciences, Beijing 100190, China

²School of Physical Sciences, University of Chinese Academy of Sciences, 19A Yuquan Road, Beijing 100049, China

³Wenzhou Institute, University of Chinese Academy of Sciences, Wenzhou, Zhejiang 325000, China

 (Received 16 October 2023; revised 18 February 2024; accepted 16 April 2024; published 16 May 2024)

Many eukaryotic microorganisms propelled by multiple flagella can swim very rapidly with distinct gaits. Here, we model a three-dimensional multiflagellate swimmer, resembling the microalgae. When the flagella are actuated synchronously, the swimming efficiency can be enhanced or reduced by interflagella hydrodynamic interactions (HIs), determined by the intrinsic tilting angle of the flagella. The asynchronous gait with a phase difference between neighboring flagella can reduce oscillatory motion via the basal mechanical coupling. In the presence of a spherical body, simulations taking into account the flagella-body interactions reveal the advantage of anterior configuration compared with posterior configuration, where in the latter case an optimal flagella number arises. Apart from understanding the role of HIs in the multiflagellate microorganisms, this work could also guide laboratory fabrications of novel microswimmers.

DOI: 10.1103/PhysRevLett.132.204002

Swimmers propelled by multiple slender appendages are ubiquitous in nature, from microorganisms [1,2] to macroscopic ones including crustaceans and feather stars [3]. These examples trigger numerous research interests in the emergence of collective motions, mediated via hydrodynamic [4–13] and steric [14] interactions, and mechanical couplings through cell body motion [15,16] and intracellular fibers [17–20]. Meanwhile, searching for optimal swimming gaits improves the understanding of biological locomotions [21–23] and inspires diverse designs of artificial microswimmers [24–29].

There are two main classes of multiflagellate microorganisms: prokaryotic cells, like bacteria *Escherichia coli* [30], and eukaryotic cells, like microalgae [18]. One fundamental question is why these microorganisms grow multiple flagella. Intuitively, cells could swim faster with more flagella. But at low Reynolds number (Re), the long-range decay of flow velocities results in strong hydrodynamic interactions (HIs), and emerging evidence indicates that HIs have a complex effect on cell motility. For prokaryotic cells, many studies have reported on the effect of HIs (see, e.g., [31] and a recent comprehensive work [32]). However, for eukaryotic cells, studies have been limited to the idealized case of two coplanar flagella [33–35]. Yet, eukaryotic cells can have more complex configurations, exemplified by algal species *Pyramimonas* [18,36,37], where up to 16 flagella are anchored at the anterior pit of the cell body beating in different crossing planes [Fig. 1(a)]. These algal cells also display distinct swimming gaits [18,38,39], including a synchronous gait with all flagella in phase and an asynchronous gait with neighboring flagella out of phase. Additionally, in an

experiment of a rotating multiflagellate swimmer, an optimal flagella number arises [25].

This accumulated evidence indicates that the HIs in multiflagellate swimmers are nontrivial and challenge the first intuition that growing more flagella would simply result in fast swimming. In this Letter, we model a microswimmer propelled by multiple eukaryotic-type flagella at low Re , combining numerical simulations and a small-amplitude analytical theory. We first show that the HIs due to the flagella motion can either enhance or impede the swimming, determined by the intrinsic flagella orientation and the phase difference between neighboring flagella. We then demonstrate the effect of the flagella-body

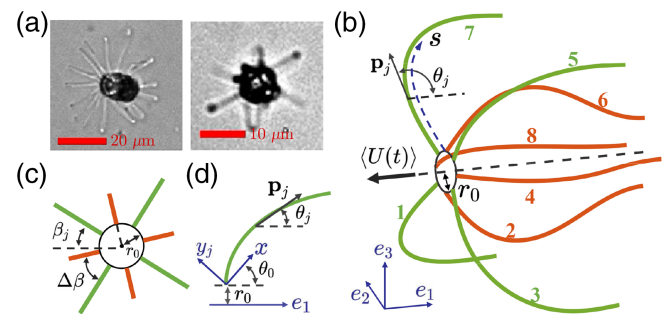


FIG. 1. (a) Swimming hexadecaflagellate *P. cyrtoptera* with synchronous gait (side view, left panel), and octoflagellate *P. octopus* with asynchronous gait (front view, right panel), adapted from [18]. (b) A multiflagellate microswimmer model with lab frame $\{e_1, e_2, e_3\}$. (c) Front view. (d) The filament frame $\{x, y_j\}$ lies in each beating plane. The filament oscillates around \hat{x} . For $\theta_0 = 0$, \hat{x} aligns with \hat{e}_1 .

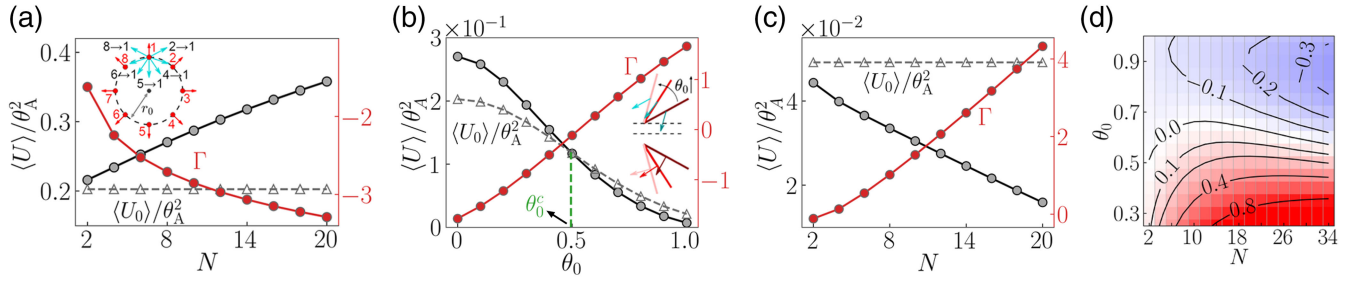


FIG. 2. Effects of HIs for synchronous gait with $r_0/L = 0.2$ ($\Gamma_0 \approx 0.2$). (a) $\langle U \rangle / \theta_A^2$ (dark circles, left axis), $\langle U_0 \rangle / \theta_A^2$ (open triangles), and Γ (red circles, right axis) versus N for $\theta_0 = 0$. (b), (c) $\langle U \rangle / \theta_A^2$, $\langle U_0 \rangle / \theta_A^2$, and Γ (b) versus θ_0 with fixed $N = 8$ and (c) versus N with fixed $\theta_0 = 0.8$. Insets of (a) and (b) show the schematics of Γ_{jk} for (a) $\theta_0 = 0$ and (b) $\theta_0 > 0$. The red arrows indicate the filament forces \mathbf{f}_k , represented as point forces, and the cyan arrows indicate $\mathbf{v}_{k \rightarrow j}$. (d) $(\mathcal{E} - \mathcal{E}_0) / \mathcal{E}_0$ versus θ_0 and N . In (a)–(c), $\theta_A = 0.2$; in (d) $\theta_A = \theta_0$.

interactions. Together, they determine the hydrodynamic advantage of multiflagellarity.

Microswimmer modeling.—We model the flagella as slender filaments of radius a , length L ($a/L \ll 1$), and bending rigidity B , moving in a Stokesian fluid of viscosity μ . We first consider a body-free swimmer, where the filaments are anchored on a frictionless circle of radius r_0 [Fig. 1(b)]. We neglect the small nonplanar component of the flagella beating for simplicity, which is responsible for the slow rotation of the cell during swimming [40], and constrain the filaments to evenly spaced two-dimensional planes [Fig. 1(c)]. To ensure a straight trajectory, the opposed filaments are always kept in phase, i.e., mirror-symmetric about the central axis, but neighboring filaments can be out of phase. The supporting circle transmits forces and constrains the ends of the filaments to move at the same velocity, resembling the mechanical coupling via the cell body [15].

The filaments are modeled as Euler-Bernoulli beams with force density $\mathbf{f}_j = -B\partial_s^4 \mathbf{r}_j + \partial_s(T\mathbf{p}_j)$, where $\mathbf{r}_j(s, t)$ is centerline position with s the arc length, \mathbf{p}_j is the tangent vector, and T is the filament tension. From a nonlocal slender-body theory, the filament dynamics is governed by a set of coupled equations [41,42],

$$8\pi\mu(\partial\mathbf{r}_j/\partial t - \mathbf{v}_j) = \Lambda[\mathbf{f}_j] + K[\mathbf{f}_j], \quad (1)$$

where $\Lambda[\mathbf{f}_j]$ and $K[\mathbf{f}_j]$ capture the local and nonlocal effects within each filament, respectively. The interflagella HIs, or direct HIs [43], \mathbf{v}_j include the nonlocal Stokeslet flows generated by all other filaments. Motivated by the bending-wave deformation of natural flagella, we assume a simple actuation mechanism by oscillating the tangent angles at the anchored points [44–46], $\theta_j(s=0, t) = \theta_A \sin(2\pi t/\tau + \phi_j) + \theta_0$, where θ_A is the amplitude, τ is the period, ϕ_j is the initial phase, and θ_0 is the intrinsic tilting angle relative to the swimming direction [Fig. 1(d)]. The importance of viscous stress compared with elastic stress on the filament is characterized by the elastoviscous number $\eta = L/(B\tau/8\pi\mu)^{1/4}$; by considering physical

parameters of natural flagella, we take $\eta = 3$ for most simulations. Equation (1) is solved numerically, subjected to the mechanical coupling at $s = 0$ and the zero-force and zero-torque constraints at $s = L$ (see Supplemental Material [47]).

Synchronous gait.—In the synchronous gait, all filaments have the identical planar deformations and bending forces. From numerical simulations based on Eq. (1), we observe that the instantaneous swimming speed $U(t)$, measured as the speed of the supporting circle, oscillates with time, but on time average the swimmer translates with a net speed $\langle U(t) \rangle$ along the $-e_1$ direction.

To analyze the swimming behavior, we first consider the case of $\theta_0 = 0$. As shown in Fig. 2(a), $\langle U \rangle$ increases with the filament number N ; but the swimming speed without incorporating HIs $\langle U_0 \rangle$ does not change with N , since the total propulsion increases in proportion to the total viscous drag as N increases. In our model, the swimming dynamics is affected by the direct HIs in two ways: the drift flow along the swimming direction $\mathbf{v}_j(s=0, t) \cdot \hat{\mathbf{e}}_1$ contributes directly to $U(t)$, and the flows perpendicular to the filaments change the filament deformations and bending forces. One can easily identify that for small tilting angles $\theta_0 \ll 1$, the drift flow is small due to the small filament forces along $\hat{\mathbf{e}}_1$. Therefore, the key to understanding the effect of HIs lies with the perpendicular flow. In order to characterize this effect, we consider the small-amplitude limit $\theta_A \ll 1$. Denote the frame translating with the filament as $\{x, y_j\}$ [Fig. 1(d)]. At the leading order in θ_A , $s \approx x$, and the planar deformations $y_j(x, t)$ satisfy the linear equations [48,54], $\xi_\perp(\partial y_j/\partial t - v_j^\perp) - f_j = 0$, where the perpendicular drag coefficient $\xi_\perp \approx 4\pi\mu/\ln(L/a)$, $v_j^\perp = \mathbf{v}_j \cdot \hat{\mathbf{y}}_j$, and the filament bending force $f_j(x, t) = -B\partial^4 y_j/\partial x^4$.

To fully describe $y_j(x, t)$, we further approximate the nonlocal Stokeslet flow using a local velocity-force relation: for the flow velocity at filament j generated by filament k ,

$$v_{k \rightarrow j}^\perp(x, t) = \mathbf{v}_{k \rightarrow j} \cdot \hat{\mathbf{y}}_j \approx \Gamma_{jk} \ln(L/r_0) f_k(x, t) / (4\pi\mu), \quad (2)$$

where Γ_{jk} denotes the coupling strength. Equation (2) is valid for $r_0/L \ll 1$. Different from the previous coplanar case [55,56], Γ_{jk} accounts for the relative orientation between the beating planes of filaments j and k . Denote $\lambda_{jk} = \cos(\beta_j - \beta_k)$ with β_j the angle between the beating plane and the $e_1 - e_2$ plane [Fig. 1(c)]. The coupling strength can be derived as [47]

$$\Gamma_{jk} = \frac{1}{2 \ln(r_0/L)} \left[1 + \lambda_{jk} \ln \left(\frac{1 - \lambda_{jk} r_0^2}{2e L^2} \right) \right], \quad (3)$$

which essentially quantifies the alignment of $v_{k \rightarrow j}^\perp$ with the motion of filament j itself: they are opposite for $\Gamma_{jk} < 0$ but aligned with each other for $\Gamma_{jk} > 0$. Then the total velocity $v_j^\perp = \sum_k v_{k \rightarrow j}^\perp = \Gamma \ln(L/r_0) f_j / (4\pi\mu)$, where the total coupling strength $\Gamma = \sum_{k \neq j}^N \Gamma_{jk} < 0$. A schematic of Γ is shown in the Fig. 2(a) inset for $\theta_0 = 0$ and $N = 8$, where Γ is negative.

By substituting v_j^\perp , we can solve for $y_j(x, t)$; with the solution, we deduce that at large η [47]

$$\langle U \rangle \sim (L/\tau) \theta_A^2 \eta^{-2} (1 + \Gamma_0 \Gamma)^{-1/2}, \quad (4)$$

where we define the intrinsic coupling strength $\Gamma_0 = \ln(L/r_0)/\ln(L/a)$. From Eq. (4), $\langle U \rangle$ increases as Γ decreases, which is verified by numerical simulations [Fig. 2(a)]. For $\Gamma < 0$, the filaments are moving against an opposing flow generated by all other filaments during both the recovery and power strokes and are bent more than those in a quiescent fluid. Consequently, the projection of the bending forces onto the swimming direction leads to an enhanced propulsion and swimming speed.

To characterize the swimming efficiency, we introduce $\mathcal{E} = D_f \langle U \rangle^2 / \langle P \rangle$ [57,58], where D_f is resistivity of a translating filament with fixed tangent angle $\theta(s) = \theta_0$ and the average power against the viscous fluid is $\langle P \rangle = \langle \int_0^L \partial \mathbf{r}_j / \partial t \cdot \mathbf{f}_j ds \rangle$. For $\theta_A \ll 1$ and $\theta_0 = 0$, $\langle P \rangle \approx \langle \int_0^L f_j \partial y_j / \partial t dx \rangle$; at large η , $\langle P \rangle \sim \theta_A^2 \eta B (\tau L)^{-1} (1 + \Gamma_0 \Gamma)^{-1/4}$. Thus the viscous dissipation is increased by HIs for $\Gamma < 0$ and decreased for $\Gamma > 0$. Combining the scaling of $\langle U \rangle$, we obtain $\mathcal{E} \sim \theta_A^2 \eta^{-1} (1 + \Gamma_0 \Gamma)^{-3/4}$, and therefore \mathcal{E} is also enhanced when Γ is negative.

For cases of $\theta_0 > 0$, $\langle U \rangle$ decreases with increasing θ_0 and becomes smaller than $\langle U_0 \rangle$ when θ_0 is larger than a critical value $\theta_0^c \simeq 0.5$ [Fig. 2(b)]. This result coincides with the geometrical dependence of the coupling strength. Since the coupling strength between neighboring filaments is always positive, the total coupling strength Γ is mainly affected by the opposed filaments. As depicted in the Fig. 2(b) inset, for an opposed pair j and k , $\mathbf{v}_{k \rightarrow j}$ induced by $f_k \hat{\mathbf{y}}_k$ is more aligned with the orientation of filament j as θ_0 increases, and at sufficiently large θ_0 , $v_{k \rightarrow j}^\perp$ turns positive. To estimate Γ in this case, we assume constant

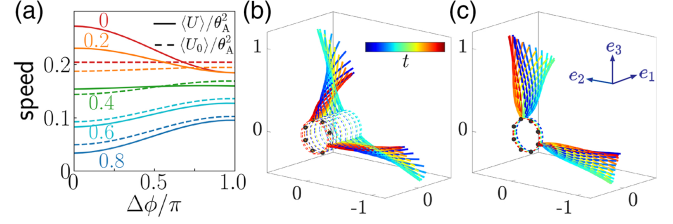


FIG. 3. Effect of asynchronous gait on swimming. (a) $\langle U \rangle / \theta_A^2$ and $\langle U_0 \rangle / \theta_A^2$ versus $\Delta\phi$ for different values of θ_0 ($\theta_0 = 0, 0.2, 0.4, 0.6$, and 0.8) with fixed $N = 8$ and $\theta_A = 0.1$. (b), (c) Time lapse of a swimmer with $N = 8$ over an actuation period for (b) $\Delta\phi = 0$ and (c) $\Delta\phi = \pi$ with $\theta_A = \theta_0 = 1.0$. Because of symmetry only two filaments are shown. Dark dots indicate the anchored positions. See Ref. [47] for simulation videos.

perpendicular force of density B/L^3 and compute \mathbf{v}_j numerically. Then, $\Gamma = [2 \ln(L/r_0)]^{-1} \eta^4 \tau L^{-2} \int_0^L v_j^\perp ds$, which increases and turns positive as θ_0 increases [Fig. 2(b)]. Meanwhile, for fixed $\theta_0 > \theta_0^c$, e.g., 0.8 , $\langle U \rangle$ decreases with N , accompanied with an increase in Γ [Fig. 2(c)]. Figure 2(d) compares \mathcal{E} with \mathcal{E}_0 , the efficiency without HIs. Across a wide range of N , $\mathcal{E} > \mathcal{E}_0$ for small θ_0 and $\mathcal{E} < \mathcal{E}_0$ for large θ_0 . In the above analysis, we have neglected the drift flow along the swimming direction, which can be important for large θ_0 and $r_0/L \rightarrow 0$. In this work, we focus on the case of $r_0/L \gtrsim 0.1$, where the effect of HIs is mainly encapsulated in Γ [47].

Asynchronous gait.—In the asynchronous gait, we set $\phi_j = \phi_{j+2}$, and neighboring filaments beat with a phase difference, $\Delta\phi = |\phi_j - \phi_{j+1}| \neq 0$. The simulation results show that the swimming speed incorporating HIs $\langle U \rangle$ is strongly affected by $\Delta\phi$. As shown in Fig. 3(a), for large $\theta_0 = 0.6$ and 0.8 , $\langle U \rangle$ increases with $\Delta\phi$; for small $\theta_0 = 0$ and 0.2 , $\langle U \rangle$ decreases with $\Delta\phi$; for intermediate $\theta_0 = 0.4$, $\langle U \rangle$ remains nearly unchanged.

The first mechanism responsible for the $\Delta\phi$ dependence is the mechanical coupling arising from the force-free condition and the rigid constraint imposed by the supporting circle, which is absent in the synchronous gait and independent from HIs. Compared to the synchronous case, the oscillatory motion of the swimmer is significantly suppressed by the mechanical coupling [Figs. 3(b) and 3(c)], consistent with experiments [28]. Physically, this is reminiscent of Huygens' coupled pendulums [59], with the difference that in our model the phase difference is fixed rather than evolving through a synchronization process. To quantify this effect, we consider a simple model of rigid filaments ($\eta \rightarrow 0$) without HIs, which cannot achieve net motion and only oscillates given imposed angular dynamics $\theta_j(t)$. Integration of Eq. (1) relates the total filament force \mathbf{F}_j with $U(t)$ and $\theta_j(t)$. By enforcing $\sum_j \mathbf{F}_j \cdot \hat{\mathbf{e}}_1 = 0$, we obtain the oscillation amplitude of the swimming speed ΔU ; in the leading order of θ_A ,

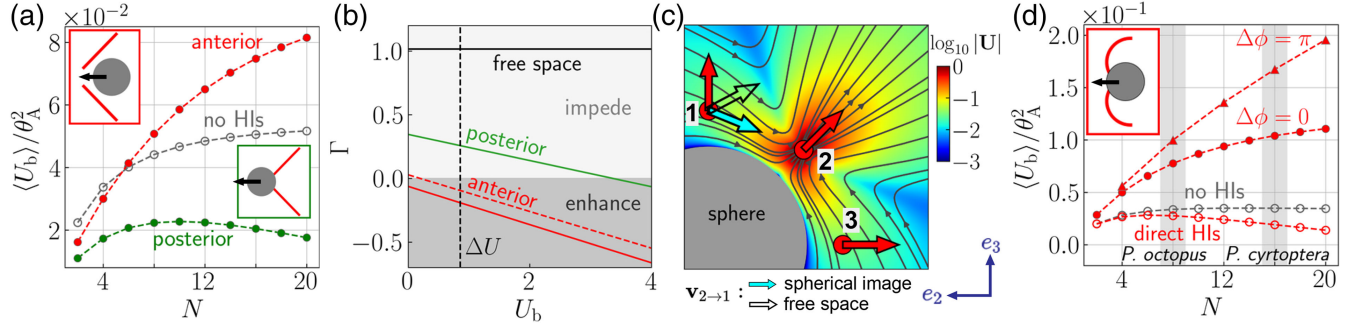


FIG. 4. Effect of spherical body for $r_0/L = 0.2$. (a) $\langle U_b \rangle$ for synchronous gait with $\theta_0 = 0.8$ and $\theta_A = 0.3$. Insets show schematics of the posterior and anterior configurations. For straight filaments, the supporting circle is separated at a fixed distance from the sphere to avoid overlapping in the anterior case. (b) $\Gamma(U_b)$ for $\theta_0 = 0.8$ and $N = 8$. The red solid and dashed lines indicate straight filaments and curved filaments with $\kappa_0 = -2.0$, respectively. The dark dashed line indicates the oscillation speed given by Eq. (5). (c) Flow field \mathbf{U} generated by the motion of filament 2. Red arrows indicate point forces. (d) $\langle U_b \rangle$ for filaments with $\kappa_0 = -2$, $\theta_0 = 2.0$, and $\theta_A = 0.8$. See Ref. [47] for videos. Circles: $\Delta\phi = 0$; triangles: $\Delta\phi = \pi$.

$$\Delta U \approx 2\pi\theta_A(L/\tau)(1 + \sin^2\theta_0)^{-1} \sin\theta_0 \cos(\Delta\phi/2). \quad (5)$$

As $\Delta\phi$ increases from 0 to π , ΔU decreases to zero. Note that $\Delta U = 0$ for $\theta_0 = 0$, which indicates that the effect of mechanical coupling is small for small θ_0 . With reduced oscillations, the speed without HIs $\langle U_0 \rangle$ increases with $\Delta\phi$ for $\theta_0 > 0$, as shown in Fig. 3(a).

By comparing $\langle U \rangle$ and $\langle U_0 \rangle$, it is now evident that the enhanced swimming speed at large θ_0 by the asynchronous gait is mainly due to the mechanical coupling. However, it cannot explain the decreasing of $\langle U \rangle$ observed at small θ_0 , where HIs dominate. Intuitively, the antiphase gait with $\Delta\phi = \pi$ turns part of the negative coupling strength Γ at small θ_0 [Fig. 2(a)] to positive by reversing the beating directions of half the filaments; since $\langle U \rangle$ is inversely related with Γ [Eq. (4)], it is decreased. An analytical calculation can be performed based on the small- θ_A approximation to quantitatively account for the effect of $\Delta\phi$ in the full range $[0, \pi]$ [47].

Loaded microswimmers.—We now examine the performance of the microswimmer with a spherical body of radius b . To satisfy the no-slip condition on the sphere, we evaluate the direct HIs \mathbf{v}_j using the spherical image system [53]. The body speed U_b is determined by balancing the filament forces with the Stokes drag $6\pi\mu b U_b$ and the additional drag due to the filament-induced flows [47,60]. Each filament also feels the flow generated by the translating sphere $\mathbf{v}_j^b(U_b)$. Therefore, following [43], the filament-body interactions, i.e., \mathbf{v}_j^b and the additional drag on the body, can be viewed as indirect HIs between filaments mediated by the body motion.

When filaments are attached at the posterior side of the body, $\langle U_b \rangle$ attains a maximum with an optimal N for the synchronous gait at a tilting angle $\theta_0 = 0.8$ [Fig. 4(a)], where the HIs have been shown to impede swimming without the sphere [Fig. 2(b)]. This is attributed to the competition between the reduced viscous load shared by

each filament as N increases and the decreased propulsion per filament due to the direct HIs. Surprisingly, $\langle U_b \rangle$ is significantly enhanced and monotonically increases with N for the anterior configuration.

To convey physical intuition, we extend the coupling strength to include the indirect HIs, $\Gamma(U_b) \sim \eta^4 \tau L^{-2} \int_0^L [v_j^\perp + \mathbf{v}_j^b(U_b) \cdot \hat{\mathbf{y}}_j] ds$, where U_b is varied to illustrate the effect of indirect HIs. The presence of the sphere changes Γ in two ways. First, the direct HIs \mathbf{v}_j , and therefore $\Gamma(0)$, are modified by the static hydrodynamic screening of the no-slip surface. For the posterior configuration, this results in a much lower $\Gamma(0)$ than that computed using the free-space Stokeslet [Fig. 4(b)]. But for the anterior configuration where the sphere is enclosed by the filaments, the distortion of the flow streamlines of neighboring filaments by the curved surface makes $\Gamma(0)$ negative. We demonstrate this effect by a cross-sectional schematic in Fig. 4(c), where $\mathbf{v}_{2 \rightarrow 1} \cdot \hat{\mathbf{y}}_1$ is clearly reversed by the curved surface. Second, the indirect HIs \mathbf{v}_j^b resist the motions of filaments for both the posterior and anterior configurations. Consequently, $\Gamma(U_b)$ decreases with U_b [Fig. 4(b)]. But for the posterior configuration, U_b is bounded by the oscillation speed without the body [Eq. (5)], and thus $\Gamma(U_b)$ remains strictly positive.

One notable feature of algal flagella is that the waveform has a static component with a nearly constant curvature [61]. To approach the actual configuration of algae, we finally perform simulations using filaments with an intrinsic curvature $\kappa_0 = -2.0$ tilted at a large angle $\theta_0 = 2.0$. Figure 4(d) shows that for the synchronous gait, an optimal N arises with only direct HIs. This is caused by the relatively large filament-sphere separation, which results in a weak distortion of the flow streamlines not sufficient to turn $\Gamma(0)$ negative [Fig. 4(b)]. Incorporating both the direct and indirect HIs leads to a significantly higher and monotonically increasing speed. The antiphase gait further enhances the swimming speed, which agrees with experiments [28].

In conclusion, we demonstrated the effect of hydrodynamic interactions between flagella on the swimming performance of a multiflagellate swimmer. Both impeding and enhancing effects are found and interpreted analytically based on the hydrodynamic coupling strength Γ . In the presence of a spherical body, our results reveal the advantage of anterior configuration compared with posterior configuration. Importantly, at large tilting angles, the direct HIs alone may not sustain a monotonic increase of speed with the flagella number N . The indirect HIs mediated by the body motion, however, regulate Γ , leading to a superior advantage of multiflagellarity. Our results have significant implications for the motility of microalgae and suggest novel designs of artificial microswimmers using soft materials [62]. The boundary-driven model assumed in this work is a significant simplification of the eukaryotic flagella [63]. While it generates a similar profile of forces acting on the fluid to natural flagella [47], combining distributed actuation with swimming dynamics needs to be addressed in future work.

The theoretical analysis presented in this work could serve as a pathway for the analysis of optimality of other multiflagellate configurations. For instance, the optimal flagella number of the rotating microswimmer [25] may be explained by computing the hydrodynamic coupling strength. The microswimmer may benefit from additional phase-shifted groups, as observed in *Pyramimonas* [18]. Indeed, asymptotic calculations without HIs have shown that three pairs of breaststrokes are sufficient to generate a steady swimming speed [45]. Last, the effect of HIs in our model of eukaryotic cells is distinct from that in bacteria. Since the motions of bacteria flagella are coupled positively via HIs within a bundle, increasing N leads to faster rotational speeds of flagella due to a relatively constant motor torque, and therefore a faster swimming speed when the body size is fixed [31]. But the linear correlation of N with the body size, combined with the collective load sharing between flagella, results in a swimming speed independent of N , or equivalently, the body size [32].

We thank Michael Shelley, Jun Zhang, and Masao Doi for helpful conversations. We thank Hugues Chaté for suggestions on the manuscript. We thank Zhaorong Liu for discussions and for providing a comparison dataset. We also thank Kirsty Wan and Raymond Goldstein for the permission to reproduce the experimental figures. This work is supported by National Natural Science Foundation of China (Grants No. 12275332, No. 12247130, and No. 12047503), China Postdoctoral Science Foundation (Grant No. 2023M743602), Chinese Academy of Sciences, Max Planck Society (Max Planck Partner Group), Wenzhou Institute (Grant No. WIUCASQD2023009), and Beijing National Laboratory for Condensed Matter Physics (Grant No. 2023BNLCPKF005).

*shiyuan.hu@itp.ac.cn

†fanlong.meng@itp.ac.cn

- [1] E. Lauga and T. R. Powers, *Rep. Prog. Phys.* **72**, 096601 (2009).
- [2] J. Elgeti, R. G. Winkler, and G. Gompper, *Rep. Prog. Phys.* **78**, 056601 (2015).
- [3] A. E. Petri, *Mesmerizing Video Shows Swimming* (National Geographic, 2016), <https://www.nationalgeographic.com/animals/article/swimming-feather-star-video-crinoid-thailand>.
- [4] N. Uchida and R. Golestanian, *Phys. Rev. Lett.* **104**, 178103 (2010).
- [5] H. Guo, L. Fauci, M. Shelley, and E. Kanso, *J. Fluid Mech.* **836**, 304 (2018).
- [6] J. Han and C. S. Peskin, *Proc. Natl. Acad. Sci. U.S.A.* **115**, 4417 (2018).
- [7] B. Chakrabarti and D. Saintillan, *Phys. Rev. Lett.* **123**, 208101 (2019).
- [8] Y. Man and E. Kanso, *Phys. Rev. Lett.* **125**, 148101 (2020).
- [9] F. Meng, R. R. Bennett, N. Uchida, and R. Golestanian, *Proc. Natl. Acad. Sci. U.S.A.* **118**, e2102828118 (2021).
- [10] B. Chakrabarti, S. Fürthauer, and M. J. Shelley, *Proc. Natl. Acad. Sci. U.S.A.* **119**, e2113539119 (2022).
- [11] A. V. Kanale, F. Ling, H. Guo, S. Fürthauer, and E. Kanso, *Proc. Natl. Acad. Sci. U.S.A.* **119**, e2214413119 (2022).
- [12] M. Tătulea-Codrean and E. Lauga, *Phys. Rev. Lett.* **128**, 208101 (2022).
- [13] D. J. Hickey, R. Golestanian, and A. Vilfan, *Proc. Natl. Acad. Sci. U.S.A.* **120**, e2307279120 (2023).
- [14] R. Chelakkot, M. F. Hagan, and A. Gopinath, *Soft Matter* **17**, 1091 (2021).
- [15] B. M. Friedrich and F. Jülicher, *Phys. Rev. Lett.* **109**, 138102 (2012).
- [16] V. F. Geyer, F. Jülicher, J. Howard, and B. M. Friedrich, *Proc. Natl. Acad. Sci. U.S.A.* **110**, 18058 (2013).
- [17] G. Quaranta, M.-E. Aubin-Tam, and D. Tam, *Phys. Rev. Lett.* **115**, 238101 (2015).
- [18] K. Y. Wan and R. E. Goldstein, *Proc. Natl. Acad. Sci. U.S.A.* **113**, E2784 (2016).
- [19] Y. Liu, R. Claydon, M. Polin, and D. R. Brumley, *J. R. Soc. Interface* **15**, 20180450 (2018).
- [20] H. Guo, Y. Man, K. Y. Wan, and E. Kanso, *J. R. Soc. Interface* **18**, 20200660 (2021).
- [21] D. Tam and A. Hosoi, *Proc. Natl. Acad. Sci. U.S.A.* **108**, 1001 (2011).
- [22] N. Osterman and A. Vilfan, *Proc. Natl. Acad. Sci. U.S.A.* **108**, 15727 (2011).
- [23] C. Eloy and E. Lauga, *Phys. Rev. Lett.* **109**, 038101 (2012).
- [24] R. Dreyfus, J. Baudry, M. L. Roper, M. Fermigier, H. A. Stone, and J. Bibette, *Nature (London)* **437**, 862 (2005).
- [25] Z. Ye, S. Régnier, and M. Sitti, *IEEE. Trans. Robot.* **30**, 3 (2013).
- [26] G. Z. Lum, Z. Ye, X. Dong, H. Marvi, O. Erin, W. Hu, and M. Sitti, *Proc. Natl. Acad. Sci. U.S.A.* **113**, E6007 (2016).
- [27] H. Lu, M. Zhang, Y. Yang, Q. Huang, T. Fukuda, Z. Wang, and Y. Shen, *Nat. Commun.* **9**, 3944 (2018).

- [28] K. Diaz, T.L. Robinson, Y.O. Aydin, E. Aydin, D.I. Goldman, and K. Y. Wan, *Bioinspiration Biomimetics* **16**, 066001 (2021).
- [29] T. Wang, H.-J. Joo, S. Song, W. Hu, C. Keplinger, and M. Sitti, *Sci. Adv.* **9**, eadg0292 (2023).
- [30] H. C. Berg, *E. coli in Motion* (Springer, New York, 2004).
- [31] F. T. M. Nguyen and M. D. Graham, *Phys. Rev. E* **98**, 042419 (2018).
- [32] S. Kamdar, D. Ghosh, W. Lee, M. Tătulea-Codrean, Y. Kim, S. Ghosh, Y. Kim, T. Cheepuru, E. Lauga, S. Lim *et al.*, *Proc. Natl. Acad. Sci. U.S.A.* **120**, e2310952120 (2023).
- [33] T. S. Singh, P. Singh, and R. Yadava, *Soft Matter* **14**, 7748 (2018).
- [34] R. Elfasi, Y. Elimelech, and A. D. Gat, *Phys. Rev. Fluids* **3**, 044203 (2018).
- [35] Z. Liu, F. Qin, L. Zhu, R. Yang, and X. Luo, *Phys. Fluids* **32**, 041902 (2020).
- [36] T. Hori and Ø. Moestrup, *Protoplasma* **138**, 137 (1987).
- [37] N. Daughbjerg and Ø. Moestrup, *Can. J. Bot.* **70**, 1259 (1992).
- [38] K. Y. Wan and R. E. Goldstein, *Phys. Rev. Lett.* **121**, 058103 (2018).
- [39] K. Y. Wan, *Phil. Trans. R. Soc. B* **375**, 20190393 (2020).
- [40] D. Cortese and K. Y. Wan, *Phys. Rev. Lett.* **126**, 088003 (2021).
- [41] R. E. Johnson, *J. Fluid Mech.* **99**, 411 (1980).
- [42] A.-K. Tornberg and M. J. Shelley, *J. Comput. Phys.* **196**, 8 (2004).
- [43] A. Chamolly and E. Lauga, *Phys. Rev. Fluids* **5**, 123102 (2020).
- [44] T. S. Yu, E. Lauga, and A. Hosoi, *Phys. Fluids* **18**, 091701 (2006).
- [45] E. Lauga, *Phys. Rev. E* **75**, 041916 (2007).
- [46] Z. Peng, G. J. Elfring, and O. S. Pak, *Soft Matter* **13**, 2339 (2017).
- [47] See Supplemental Material at <http://link.aps.org/supplemental/10.1103/PhysRevLett.132.204002> for simulation videos, numerical and analytical details, which includes Refs. [17,35,38,46,48–53].
- [48] C. H. Wiggins, D. Rivelino, A. Ott, and R. E. Goldstein, *Biophys. J.* **74**, 1043 (1998).
- [49] S. Hu, J. Zhang, and M. J. Shelley, *Soft Matter* **18**, 3605 (2022).
- [50] S. Hu and F. Meng, *J. Fluid Mech.* **966**, A23 (2023).
- [51] G. Xu, K. S. Wilson, R. J. Okamoto, J.-Y. Shao, S. K. Dutcher, and P. V. Bayly, *Biophys. J.* **110**, 2759 (2016).
- [52] D. R. Brumley, K. Y. Wan, M. Polin, and R. E. Goldstein, *eLife* **3**, e02750 (2014).
- [53] S. Kim and S. J. Karrila, *Microhydrodynamics: Principles and Selected Applications* (Courier Corporation, New York, 2013).
- [54] C. H. Wiggins and R. E. Goldstein, *Phys. Rev. Lett.* **80**, 3879 (1998).
- [55] R. E. Goldstein, E. Lauga, A. I. Pesci, and M. R. E. Proctor, *Phys. Rev. Fluids* **1**, 073201 (2016).
- [56] Y. Man, L. Koens, and E. Lauga, *Europhys. Lett.* **116**, 24002 (2016).
- [57] M. J. Lighthill, *Commun. Pure Appl. Math.* **5**, 109 (1952).
- [58] L. E. Becker, S. A. Koehler, and H. A. Stone, *J. Fluid Mech.* **490**, 15 (2003).
- [59] A. Pikovsky, M. Rosenblum, and J. Kurths, *Synchronization: A Universal Concept in Nonlinear Science* (Cambridge University Press, Cambridge, 2001).
- [60] J. J. Higdon, *J. Fluid Mech.* **90**, 685 (1979).
- [61] V. F. Geyer, P. Sartori, B. M. Friedrich, F. Jülicher, and J. Howard, *Curr. Biol.* **26**, 1098 (2016).
- [62] H. Zhou, C. C. Mayorga-Martinez, S. Pané, L. Zhang, and M. Pumera, *Chem. Rev.* **121**, 4999 (2021).
- [63] W. Gilpin, M. S. Bull, and M. Prakash, *Nat. Rev. Phys.* **2**, 74 (2020).